Computational Modeling and Simulation of Gas Turbulence Phenomena in Solution Blow Spinning Process for Ceramic Nanofibers

Camila Ariana Becker Pereira[1], Maria Dennise Medeiros Macêdo[2], Romualdo Rodrigues Menezes[3], Severino Rodrigues de Farias Neto[4]

[1,2,3] Department of Materials Engineering, Federal University of Campina Grande, 58429-900 Campina Grande, Brazil

[4] Department of Chemical Engineering, Federal University of Campina Grande, 58429-900 Campina Grande, Brazil

[1] camilabeckerp@farmace.com.br
[2] dennisemed1@gmail.com
[3] romualdomenezes@gmail.com
[4] severino.rodrigues@eq.ufcg.edu.br

ABSTRACT

The high-speed air profile expelled from a solution blow spinning nozzle was investigated using computational fluid dynamics and a k-ε turbulence model. A convergent nozzle comprised of a polymer solution channel, an air inlet and an air chamber were computationally generated to better understand the behavior of the fluids inside the matrix. Three meshes were proposed to study the influence of air velocity, pressure, and turbulent kinetic energy. The variation in gas outlet velocity reveals a lack of uniformity in the profile, indicating that the tube length is insufficient to achieve uniformity, which may significantly impact fiber morphology. Under different pressures (40 and 30 psi), there was a reduction in the average gas velocity inside and at the tube outlet. However, uniformity has not yet been achieved, potentially affecting fiber continuity.

KEYWORDS: Computational Fluid Dynamics, Solution Blow Spinning, Ceramic Nanofibers.

I. INTRODUCTION

With the emergence of nanotechnology, in-depth research has been carried out to create fibers with smaller diameters, particularly within the range of nanometers and submicrometers. Ceramic nanofibers, in particular, have garnered substantial interest in the realm of materials science due to their broad spectrum of possible applications in advanced ceramic materials. Multiple domains, including catalysis, sensors, and biomaterials, have showcased remarkable outcomes, underscoring the significant promise held by this category of material.[1]–[3].

While electrospinning remains the prevailing method for producing nanofibers, it is not exempt from its inherent constraints. One of the principal drawbacks of this approach is its limited fiber output, a factor that impedes its real-world usability [4], [5]. However, in response to these limitations, the Solution Blow Spinning (SBS) technique has emerged as a highly promising alternative for nanofiber production. SBS incorporates principles from various polymeric spinning techniques, such as "air jet spinning," making it an efficient and user-friendly method for spinning nanofibers. The process involves the controlled deposition of a polymer solution or melt through a nozzle, followed by the application of a high-speed gas stream to induce fiber formation[6]–[8].

In recent years, significant efforts have been made to investigate the dynamics of fiber formation and the effects of processing parameters on fiber morphology in blown solution spinning, as evident in studies conducted by Gugulothu et al[9]. Nevertheless, even with the broad enthusiasm and swift advancement in this methodology, our comprehension of turbulent airflow patterns, both in theoretical and experimental contexts, remains inadequate. This lack of understanding can be attributed to the

intricate aerodynamic interactions manifested by the air jets or gases employed in the procedure. Consequently, attaining a thorough grasp of the dynamics governing airflow becomes crucial for refining the SBS technique and attaining meticulous command over the ultimate nanofiber structure [10], [11].

Computational Fluid Dynamics (CFD) presents a robust means to thoroughly examine and comprehend the complex mechanisms inherent in SBS. By harnessing CFD simulations, scientists can replicate and scrutinize intricate fluid flow patterns, turbulence attributes, and the interplay between gas jets and polymer solutions/melts. Through numerical simulations, CFD facilitates the visualization and measurement of airflow dynamics, furnishing invaluable understandings into the conduct of air jets and their influence on fiber creation. This enables the fine-tuning of process variables, including gas flow rate, nozzle configuration, and positioning, for the optimization of outcomes [12]–[14].

In this study, Computational Fluid Dynamics and a k-ε turbulence model were employed to examine the flow characteristics of high-speed air expelled from a solution blow spinning nozzle. To gain insight into the fluid behavior within the system, the processing variables and their influences for solution blow spinning were investigated, using the Ansys Fluent computational fluid dynamics tool. Initially, simulations and mathematical modeling were developed and subsequently the numerical solution of the differential equations that describe the problem was performed. In the study, were considered a three-dimensional, incompressible and without heat transfer turbulent flow regime.

II.   EXPERIMENTAL

2.1. Physical Problem Definition

The Solution Blow Spinning (SBS) technique utilizes various systems for spinning nanofibers, which encompass modifications in the solution ejector needle and the compressed air ejector tube, as well as adjustments in processing conditions that have a direct influence on the resulting nanofiber morphology. Previous research has primarily concentrated on simulating the fiber formation process subsequent to ejection into the drying medium, regardless of whether it is heated or not[15], [16].

However, a research gap exists when it comes to understanding the dynamics within the matrix, specifically concerning the behavior of air and solution flow within the tubes. The air flow inside the matrix can manifest as either linear or turbulent, with distinct velocity gradients, exerting a significant impact on the formation of nanofibers[17], [18].

The noozle matrix used in this work is illustrated in Figure 1. The dimensions were measured using the ImageJ software.

**Figure 1.** Solution blow spinning (SBS) nozzle

The spinning process using Solution Blow Spinning (SBS) encompasses multiple steps and components. Figure 2 illustrates the two distinct domains available for studying SBS, represented by green and red colors. The first domain encompasses the spinning matrix, with the gas inlet positioned perpendicular to the spinning tube, the linear entry of the solution into the spinning tube, and the

ejector nozzle that features a spacing known as protrusion, relative to the main tube. Within this first domain, an analysis will be conducted to investigate the behavior of the gas within the spinning matrix. The second domain is situated beyond the exit point of the spinning solution and gas from the matrix, where they enter the medium where the subsequent drying process occurs. However, this particular domain will not be addressed in the context of this study.
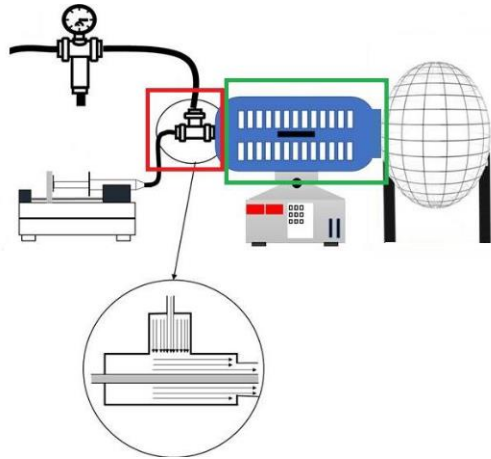
Figure 2. SBS setup for the production of ceramic fibres. The first and second domains are pointed in green and

red, respectively

Figure 3a displays a cross-sectional view of the annular coaxial injector nozzle, which is widely utilized in solution blow spinning. This two-dimensional model illustrates the injection process. The inner nozzle (needle) is responsible for pumping the polymer solution, while the concentric outer tube allows the passage of pressurized air. As the gas flows, it exerts a significant drag force, which elongates and stretches the solution jet.
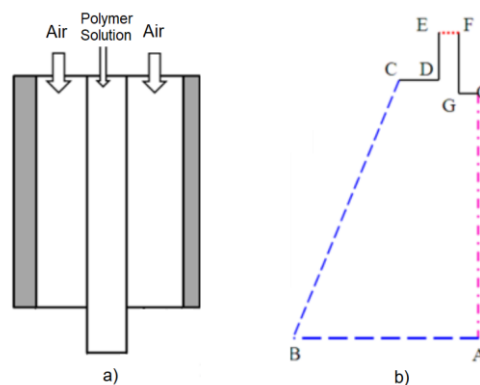
Figure 3. (a) 2D Model of wiring wolution nozzle (cross-sectional view), and (b) the computational area of

study

The k-ε turbulence model is commonly used in CFD to simulate the flow characteristics under turbulent flow conditions. To optimize the airflow field for spinning solution, the orthogonal array design method was employed. This experimental technique allows for increased productivity and quality with minimal trials. It utilizes partial factor analysis.

Previous works[19] have noted the significance of nozzle geometry in the wiring solution process, affecting the distribution of air flow, air speed, and fiber morphology. In this study, in addition to investigating the influence of the matrix beak, internal events within the matrix were also explored.

Study Domain 1 is composed of the nanofiber spinning matrix, which consists of two main concentric tubes and an outer tube perpendicular to them, serving as the gas inlet (Figure 4a). Pressurized gas flows through the matrix between the two tubes and only comes into contact with the spinning solution at the end, near the spinning spout. The gas inside the matrix can exhibit turbulent behavior due to high pressures, resulting in varying velocity and pressure profiles within it. The velocity profile may exhibit uniformity or non-uniformity, leading to significant consequences in the spinning process. When the gas interacts with the solution, it can deform the jet in different ways, consequently affecting its morphology (Figure 4b). On the other hand, the behavior of the solution can be considered linear since its entry occurs within the central tube of the spinning matrix (Figure 4c).
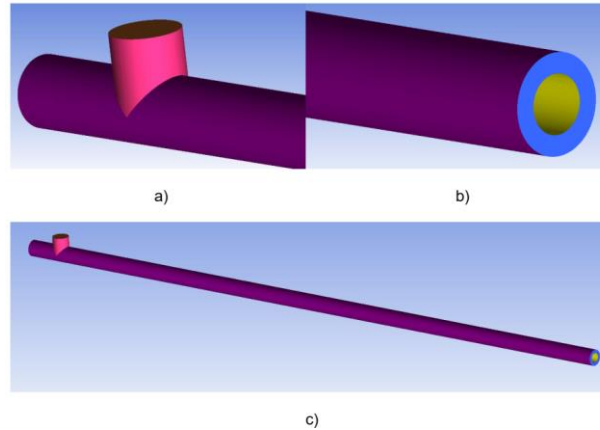
Figure 4. (a) Pressurized gas and polymer solution inlet, (b) matrix outlet, and (c) matrix body

2.2. Mesh Convergence Index (CMI)

To determine the mesh convergence index and quantify the uncertainties related to discretization errors, and consequently identify the optimal mesh that does not impact the obtained results, an initial representative mesh size h is determined, as seen Equation (1)[20].

$$h = \left[\frac{1}{N} \sum_{i=1}^{N} \Delta V_i \right]^{1/3}$$

$$(1)$$

Where N is the number of elements in the mesh used for computational calculations, and ΔV_i is the volume occupied by element i. Three meshes are adopted, with $h1 < h2 < h3$, and the mesh refinement ratios $r_{21} = h_2 / h_1$ and $r_{32} = h_3 / h_2$ are chosen such that the mesh refinement is done systematically and the ratio is greater than 1.3. Since the refinement ratios differ, the order of convergence is calculated using the refinement ratio between the finest and intermediate mesh, and between the intermediate and coarsest mesh.

2.3. Boundary conditions and governing equations

The experimental data from the wiring of nanofibers was used under the following conditions: compressed air as the gas and pressure of injection of 344,738 Pa. The viscosity and density data of compressed air were obtained from the program catalog, with values of 1.7894×10^{-5} kg/m^{-s} and 1.225 kg/m^3, respectively. The turbulent k-ε method was employed, using the Standard conditions, with a residual value between simulation iterations below 10^{-7}. One thousand iterations were performed on each mesh to achieve data convergence.

In order to complete the mathematical model, the following boundary conditions were defined for the turbulent single-phase flow:

$$u = v = 0 \text{ and } w = U \text{ gas} \neq 0 \text{ for } \forall(x, y)$$

A uniform and constant inlet pressure value was adopted, with x, y and z wall velocities set to zero. Figure 5 shows the gas inlet, wall region and the gas outlet of the matrix.
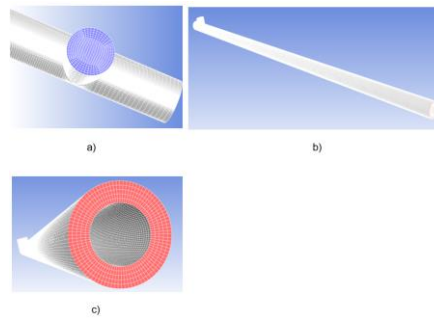

Figure 5. (a) Gas inlet, (b) wall region, and (c) gas outlet of the matrix

To better summarize the characteristics adopted for the resolution of the mathematical model and numerical treatment in this work, Table 1 displays the adopted parameters and set parameters used.

Table 1. Conditions adopted for solving the governing equations

Conditions	Applied parameters
Flow mode	Single-phase (gas), three-dimensional, incompressible and isothermal
Interface Transfer Model	k-ε turbulence model
Gravitational force	Considered
Residual Convergence Criterion	10^{-7}
Treatment near the wall	Standart

III.   RESULTS AND DISCUSSION

3.1. Dimensions of the nozzle matrix

The diameters of the nozzle (D), of the needle (d) and the length of the protrusion of the needle (L) were then determined in millimeters and are presented in Table 2. Meanwhile, Table 3 displays the dimensions of the whole spinning matrix.

Table 2. Dimensions of the spinning die nozzle

Needle diameter (d)	Nozzle diameter (D)	Length of needle putrus (L)
1.346 mm	2.283 mm	1.783 mm

Table 3. Wiring Matrix Dimensions

Conditions	Set parameters
Diameter of the larger tube (A)	2.283 mm
Displacement of the gas inlet tube (B)	3.8585 mm
Diameter of the gas inlet tube (C)	2.283 mm
Height of the gas inlet tube (D)	1.359 mm
Total length of the matrix (E)	100.000 mm
Diameter of the smaller tube (F)	1.783 mm

The dimensions of the wiring matrix are depicted in the plan, on the xy axes, shown in Figure 6. In Figure 6a, a section of the gas injection region is displayed, illustrating its position at the entry point of the spinning tube. Figure 6b presents the whole SBS matrix, maintaining the proportions, with the area highlighted in blue representing the region under study in this work. This blue area corresponds to the regions through which the pressurized gas will flow.
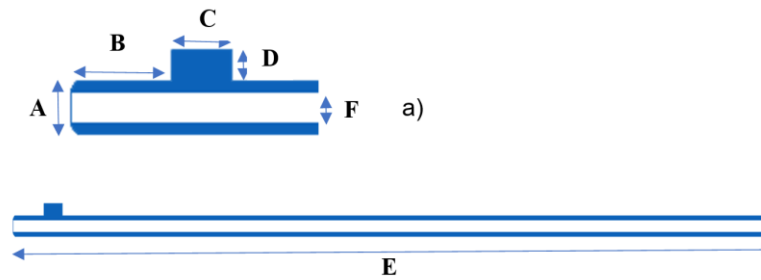
Figure 6. (a) Gas injection region, (b) SBS matrix

The meshes for the blow solution spinning matrix were analyzed to solve the mass conservation, linear momentum and energy conservation equations. In addition to the boundary conditions described in the previous section, the gas inlet pressure was set as 344,738 Pa; ambient gas outlet pressure and gravity of 9.81 m/s^2.

To analyze the behavior of the variables of interest (velocity and pressure), horizontal lines were drawn in three axial positions along the length of the computational domain: at 10 mm; 55 mm and 100 mm (gas outlet). With regard to the effect of the mesh on the results of the spinning process in the matrix, the mathematical model based on the Navier-Stokes equations was used, using the k-ε turbulent systems model[21]. For this, the considerations previously described for the mathematical modeling of the flow in the SBS matrix were used. It was also taken into account that they describe the conservation of mass and linear momentum. The physicochemical properties of the gas (compressed air) were used as standard from the Fluent simulation program.

3.2. MCI - Average Gas Velocity

Table 4 presents the results of the convergence study for the average air velocity at the matrix gas outlet. This region was selected because it is the position where the compressed gas would come into contact with the spinning solution, the other positions of interest were analysed and have their results shown in Table 5 and Table 6, in the central and initial region, respectively.

Table 4. Results of the mesh convergence study for air velocity at the gas outlet

M_1 (m/s)	M_2 (m/s)	M_3 (m/s)	ϕ_{21} ext (m/s)	MCI_{21} (%)	MCI_{32} (%)	C	$r^p MCI_{21}$
340.676	340.693	351.684	340.675	0.00024	0.00648	0.00155	0.00648

Table 5. Results of the mesh convergence study for air velocity in the central region of the matrix

M_1 (m/s)	M_2 (m/s)	M_3 (m/s)	ϕ_{21}ext (m/s)	MCI_{21} (%)	MCI_{32} (%)	C	$r^p MCI_{21}$
340,778	340,794	351,823	340,777	0,00061	0,00609	0,00145	0,00609

Table 6. Results of the mesh convergence study for air velocity in the initial region of the matrix

M_1 (m/s)	M_2 (m/s)	M_3 (m/s)	ϕ_{21}ext (m/s)	MCI_{21} (%)	MCI_{32} (%)	C	$r^p MCI_{21}$
336,695	336,682	347,68	336,679	0,00582	0,05295	0,01169	0,05297

An improvement in the convergence condition is evident, with MCI_{21} and MCI_{32} values falling within the 10% limit as reported by Karatekin[21]. This indicates a reduced dependence of the results on the mesh element size and suggests a convergence towards a mesh-independent solution. In line with the findings of Paudel and Saenger[22], the value of C confirms the monotonous convergence of the solution in all three regions, thus reinforcing the consistency of the results. Notably, the close values of MCI_{32} and $rpMCI_{21}$ suggest that the extrapolated solution closely approximates the exact solution of the variable. These consistent findings are replicated across all three analyzed regions.

It can be observed that as the mesh becomes more refined, the solution approaches the asymptotic value of the extrapolated solution. The solution obtained with Mesh M_1 exhibits the closest agreement, while Mesh M_2 also demonstrates satisfactory results that approach the extrapolated solution, and at the same time requires less simulation time compared to Mesh M_1. The extrapolated

solution represents an estimated value of the exact solution for the compressed air velocity. Figure 7 illustrates the graph depicting the gas velocity in each region of the spinning tube, revealing that both Mesh 1 and Mesh 2 closely match the estimated values across all regions of interest in the tube study.
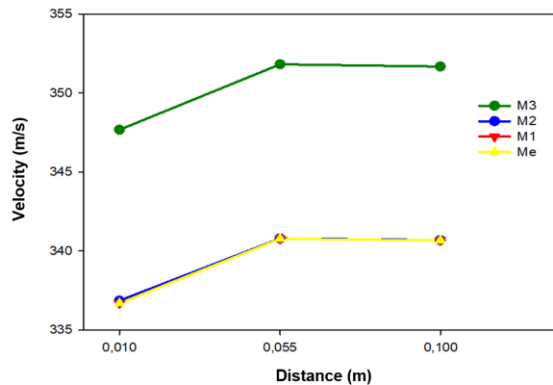

Figure 7. Comparison of meshes regarding gas velocity in different regions

Figure 8a provides an overview of the velocity profile along the tube for Mesh 1. It reveals a notable variation in the velocity gradient at the junction of the pressurized gas inlet tube and the central tube of the wiring matrix. In Figure 8b, as the flow progresses through the tube, this gradient smoothes out and tends towards uniformity.
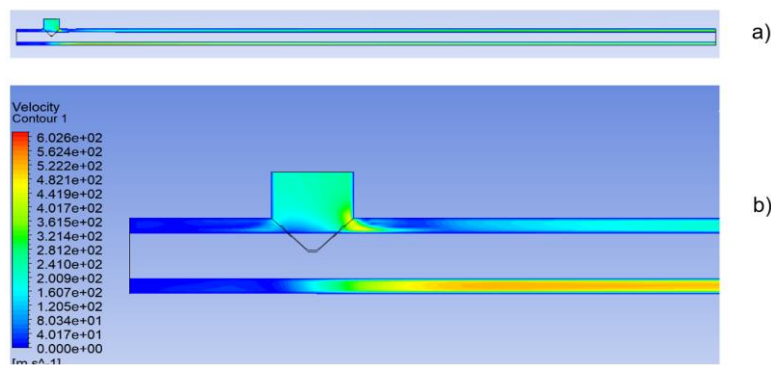

Figure 8. Velocity gradients during gas injection in M1

Figure 9 illustrates the compressed air velocity profiles within the gas matrix in the three different regions of interest for M_1. The higher velocities are measured at the gas inlet in the spinning tube, with higher velocities at the bottom of the tube. Moving to the intermediate region of the tube, there is an average decrease in the velocity profile, with an increase of the gas velocity in the upper part and decrease in the lower part, still without profile uniformity. At the exit of the tube the gas apparently remains with the same velocity and with a more homogeneous profile in the sectioned region.
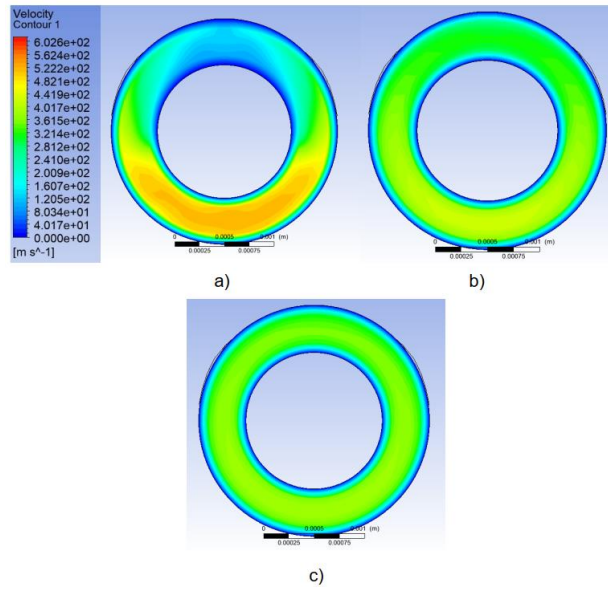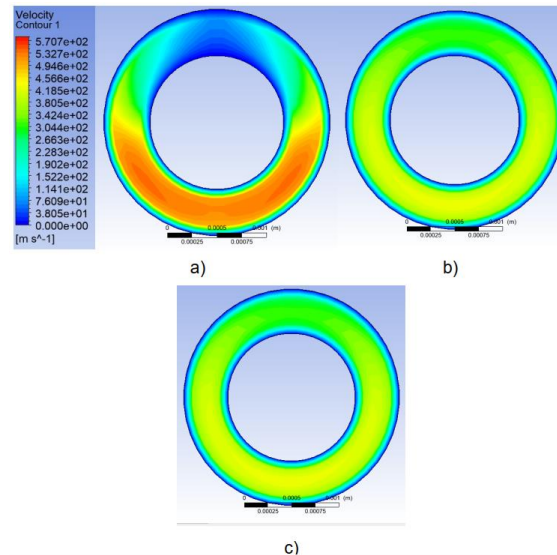
Figure 9. Compressed air velocity profiles inside the gas matrix in the three different regions of mesh 1

Meshes M_2 and M_3, shown in Figures 10 and 11, respectively, follow the same trend as mesh M_1 in the three regions chosen for analysis.
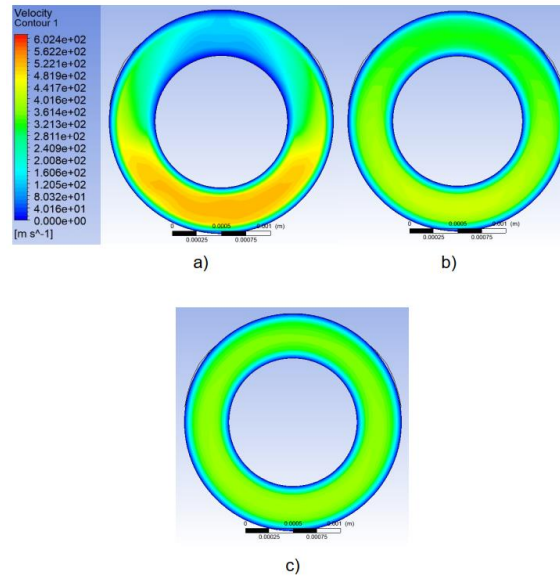
Figure 10. Compressed air velocity profiles inside the gas matrix in the three different regions of mesh 2

Figure 11. Compressed air velocity profiles inside the gas matrix in the three different regions of mesh 3

Mesh M_2 presents a velocity profile very similar to that of mesh M_1, which corroborates the mesh convergence index data. It suggests that the two meshes have similar behavior, and where M_2 could already be used as a mesh of study. The M_3 mesh, being the least refined, is the one that is most distant from the measured results, with a profile of higher velocities throughout the gas tube and presenting homogeneity at the tube outlet.

Apparently in the gas exit region there is uniformity in the velocity profile, even for M_1; but drawing a line perpendicular to the X axis at a distance of 99 mm from the origin, and with height varying from +/- 1.14 mm, it is possible to analyze in more detail what happens in this region, as can be seen in Figure 12 for Mesh 1.
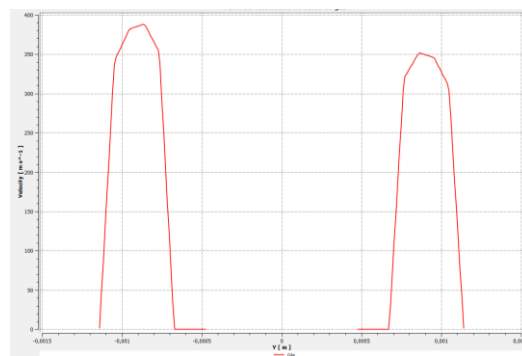
Figure 12. Velocity at gas outlet M_1 at (99, 1.14 mm) x,y coordinates

For Mesh 1 at the gas outlet, there is a velocity difference between the lower region of the tube and the upper one, where in the lower region the gas is at greater speed, surpassing the opposite region of the tube by approximately 36.8 m/s.

This shows that the size of the tube was still not enough to standardize and linearize the air flow inside it, and this can strongly interfere with the morphology of the nanofibers[15].

3.3. MCI - Gas Pressure

Table 7 displays the results of the convergence study for air pressure in the initial region of the matrix. This particular region was chosen due to its significant pressure distribution gradient. Additionally, the results for the central region can be found in Table 8. However, the final region of the tube was not evaluated as it assumes ambient pressure outside the tube.

Table 7. Results of the mesh convergence study for air pressure in the initial region of the matrix

| M_1 (m/s)	M_2 (m/s)	M_3 (m/s)	$\phi_{21}\,ext$ (m/s)	MCI_{21} (%)	MCI_{32} (%)	C	$r^p\,MCI_{21}$
159,346	159,359	161,32	159,344	0,00090	0,01109	0,00663	0,0111

Table 8. Results of the mesh convergence study for air pressure in the central region of the matrix

M_1 (m/s)	M_2 (m/s)	M_3 (m/s)	$\phi_{21}\,ext$ (m/s)	MCI_{21} (%)	MCI_{32} (%)	C	$r^p\,MCI_{21}$
87,892	87,899	93,12	87,892	0,00036	0,01032	0,00134	0,01032

A reduction in the convergence conditions is observed, and according to Karatekin [20], the values of MCI_{21} and MCI_{32} are within a 10% range. This indicates a reduced dependence of the results on the size of the mesh elements, approaching a mesh-independent solution. Confirming the findings of Paudel and Saenger[22], the value of C indicates the monotonic convergence of the solution in three different regions, thus validating the results.

Moreover, it can be observed that the finer the mesh, the closer the solution is to the asymptotic value of the extrapolated solution. While the M_1 mesh yields the closest results, the M_2 mesh also provides satisfactory outcomes with a lower simulation time compared to the M_1 mesh. The extrapolated solution represents an estimated value of the exact compressed air pressure solution.

In Figure 13a, a general view of the pressure distribution throughout the piping of Mesh 1 is shown. At the intersection between the pressurized gas inlet piping and the central piping of the wiring matrix, there is a noticeable variation in the pressure gradient, as depicted in Figure 13b. However, this gradient smooths out and tends to become more uniform as the air travels along the tube.
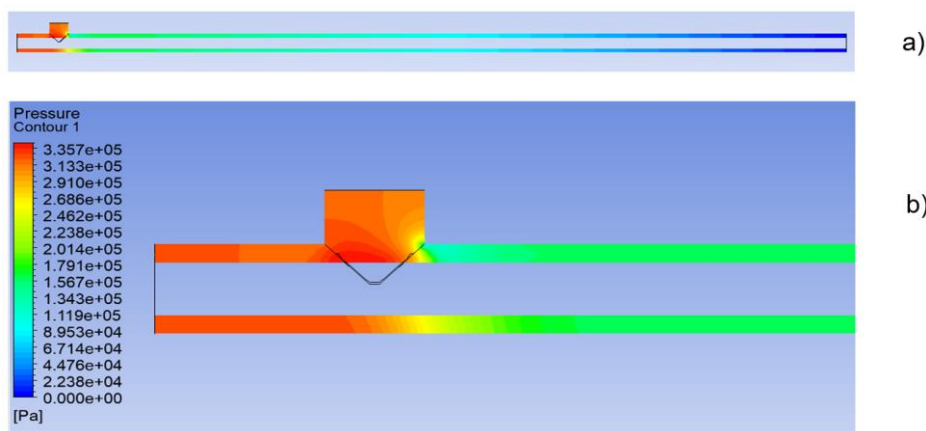
Figure 13. Pressure gradients during gas injection in M_1

It is crucial to highlight that the pressure, although it has minimal influence on the diameter of micro/nanostructures, needs to be carefully adjusted to ensure a continuous polymeric jet [23], [24]. Upon observing the results of the mesh convergence index and analyzing the velocity and pressure profiles at different points, two meshes stand out as they exhibit satisfactory results and closely match the expected values. These meshes provide sufficient accuracy to achieve the desired simulated outcomes while also reducing the simulation time.
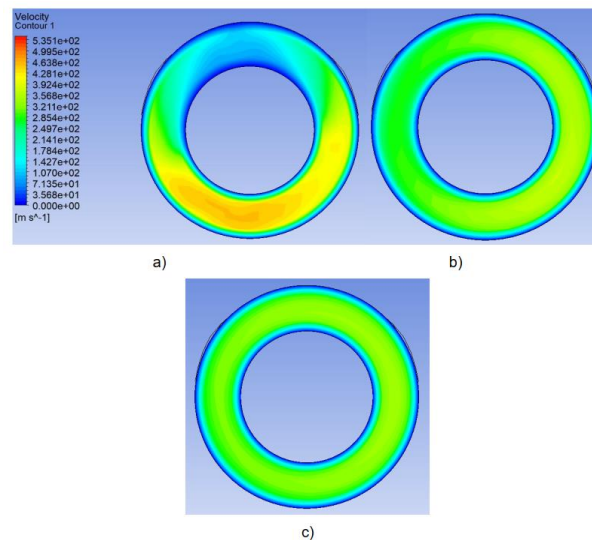
3.4. Velocity Profile at 40 Psi

Simulations were conducted with two additional pressure settings to examine whether the uniformity of gas velocity could be achieved by reducing the gas inlet pressure. Pressures of 40 Psi (275,790 Pa) and 30 Psi (206,843 Pa) were selected, while maintaining the same boundary conditions as the previous simulations and applying them to Mesh 2. The analysis focused on three different regions throughout the matrix.

Figure 14a provides an overview of the velocity distribution throughout the entire pipe of Mesh 2. Notably, a significant variation in the velocity gradient is observed at the junction of the pressurized gas inlet tube and the central tube of the spinning array, as depicted in Figure 14b. However, as the air progresses through the tube, this gradient gradually smoothes out and approaches a more uniform velocity profile.
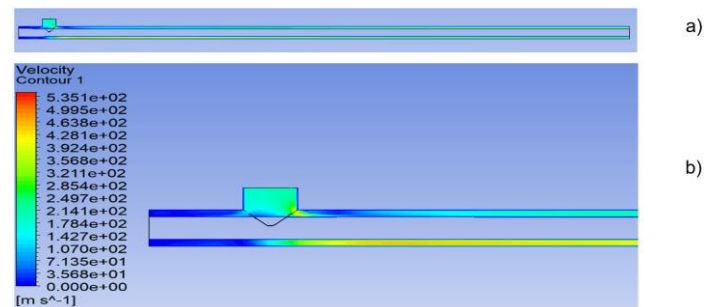

Figure 14. Velocity gradients during gas injection at 40 psi

Figure 15 illustrates the distribution of compressed air velocity within the gas matrix across three distinct areas of interest: near the gas inlet (10 mm), midway along the tube (55 mm), and at the gas outlet of the matrix. It is evident that the velocity measured at the gas inlet of the rotating tube is higher, and there is an increased velocity at the bottom of the tube, as depicted in Figure 15a. As the air travels towards the middle region of the tube, the velocity distribution gradually decreases uniformly, as shown in Figure 15b. At the tube exit, the gas maintains a relatively consistent velocity and exhibits a more uniform velocity profile across the tube's cross-sectional area, as depicted in Figure 15c.

Figure 15. Compressed air velocity profiles inside the matrix in the three different regions at 40 Psi

In the gas outlet the velocity distribution appears to be nearly uniform, as depicted in Figure 15c. However, for a more detailed analysis, a line perpendicular to the X-axis was drawn, located at a distance of 99 mm from the origin, with a height of +/- 1.14 mm. This allowed for a more in-depth evaluation of the actual situation in this specific region, as shown in Figure 16.
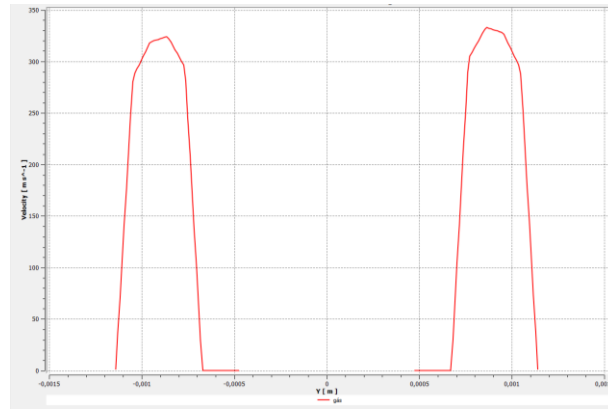
Figure 16. Velocity at gas outlet at (99, 1.14 mm) x,y coordinates, 40psi

At 40 Psi, there is a noticeable velocity disparity between the lower and upper regions of the tube. Specifically, in the upper region, the gas exhibits a higher velocity, surpassing the velocity in the opposite region of the tube by approximately 8.96 m/s. This discrepancy indicates that the current tube size and pressure are insufficient to achieve a standardized and linearized airflow inside it. Such variations in airflow may have implications for the morphology of the nanofibers being produced[15].
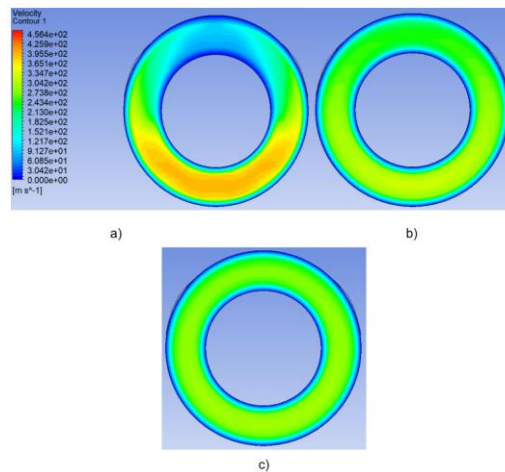
3.5. Velocity Profile at 30 Psi

Figure 17a provides a comprehensive view of the velocity distribution across all pipes in Mesh 2. Figure 17b highlights the region where the pressurized gas inlet tube intersects with the central tube of the spinning matrix, revealing a significant variation in the velocity gradient. However, as the air progresses through the matrix, this gradient smoothes out and approaches a presumed uniformity at the outlet.
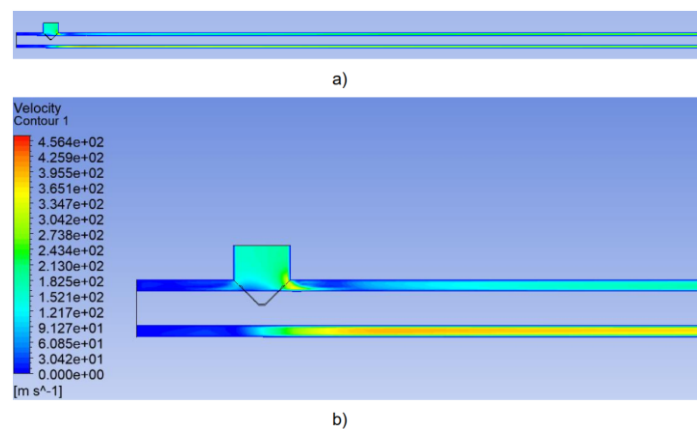

Figure 17. Velocity gradients during gas injection at 30 psi

Figure 18 depicts the distribution of compressed air velocity within the gas matrix across three different regions of interest. It is evident that the velocity measured at the air inlet of the central tube is higher. Additionally, there is a greater velocity at the bottom of the tube, as illustrated in Figure 18a. As the air progresses towards the central region of the tube, the velocity distribution in this area decreases uniformly. Notably, the velocity of the rising gas decreases from top to bottom, as depicted in Figure 18b. At the exit of the tube, the gas maintains a relatively constant velocity and exhibits a more uniform velocity profile in the cross-sectional area of the tube, as shown in Figure 18c.

Figure 18. Compressed air velocity profiles inside the matrix in the three different regions at 30 Psi

In the gas outlet region, a uniform velocity profile is observed, as depicted in Figure 18c. However, for a more detailed analysis, a line perpendicular to the X-axis was drawn at a distance of 99 mm from the origin, with a height ranging from +/- 1.14 mm. This enables a closer examination of the phenomena occurring in this specific region, as depicted in Figure 19.
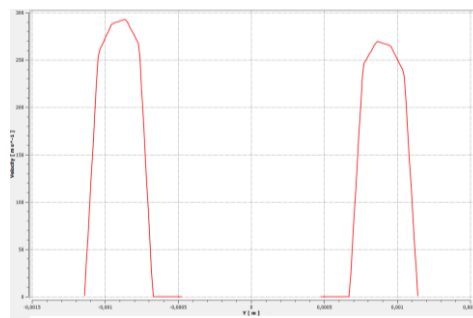
Figure 19. Velocity at gas outlet at (99, 1.14 mm) x,y coordinates, 30psi

At 30 Psi, there is a notable difference in velocity between the lower and upper regions of the tube. Specifically, in the lower region, the gas exhibits a higher velocity, surpassing the velocity in the opposite region of the tube by approximately 23.47 m/s. The studies conducted at these two different pressures indicate a decrease in the average velocity at the tube exit and along its path. Furthermore, smaller differences in velocity were observed between the upper and lower regions of the tubes. However, these findings cannot conclusively determine the overall impact on spinning morphology, as low velocities may lead to discontinuity in the ceramic nanofibers.

IV. CONCLUSIONS

The current work provides a comprehensive numerical analysis for ceramic nanofibres produced by solution blow spinning. The flow characteristics of high-speed air through a nozzle were investigated numerically using computational fluid dynamics, with three distinct meshes for the spinning die body. The mesh convergence index was calculated in three different regions of the spinning die tube, demonstrating reduced dependence on mesh element size and proximity to a mesh-independent solution in the studied variables and regions. The estimated C value indicated monotonic convergence of the solution in all three regions. The mathematical model accurately described the three-dimensional gas flow behavior within the spinning die. Two meshes emerged as promising candidates for future work, M1, and M2, closely approaching expected results. The second mesh, M2, was chosen for further study due to its satisfactory results, according to the extrapolated values in the mesh convergence index, velocity and pressure profiles, and reduced computational time. The velocity distribution at the gas outlet showed non-uniformity, suggesting insufficient tube length for standardization and potential impact on fiber morphology. Varying the pressure (40 and 30 Psi)

resulted in decreased average gas velocity inside and outside the tube, but uniformity had not yet been achieved, potentially affecting fiber continuity.

ACKNOWLEDGEMENTS

REFERENCES

[1]   J. Xue, T. Wu, Y. Dai, and Y. Xia, "Electrospinning and electrospun nanofibers: Methods, materials, and applications," *Chem. Rev.*, vol. 119, no. 8, pp. 5298–5415, Apr. 2019.

[2]   M. S. Islam, B. C. Ang, A. Andriyana, and A. M. Afifi, "A review on fabrication of nanofibers via electrospinning and their applications," *SN Appl. Sci.*, vol. 1, no. 10, pp. 1–16, Oct. 2019.

[3]   D. Yadav, F. Amini, and A. Ehrmann, "Recent advances in carbon nanofibers and their applications – A review," *Eur. Polym. J.*, vol. 138, p. 109963, Sep. 2020.

[4]   Y. Li *et al.*, "Developments of Advanced Electrospinning Techniques: A Critical Review," *Adv. Mater. Technol.*, vol. 6, no. 11, p. 2100410, Nov. 2021.

[5]   X. Zhang, X. Wang, W. Jiao, Y. Liu, J. Yu, and B. Ding, "Evolution from microfibers to nanofibers toward next-generation ceramic matrix composites: A review," *J. Eur. Ceram. Soc.*, vol. 43, no. 4, pp. 1255–1269, Apr. 2023.

[6]   K. G. de C. Monsores, A. Oliveira da Silva, S. de S. A. Oliveira, R. P. Weber, and M. L. Dias, "Production of nanofibers from solution blow spinning (SBS)," *J. Mater. Res. Technol.*, vol. 16, pp. 1824–1831, Jan. 2022.

[7]   F. T. G. Dias, S. P. Rempel, L. D. Agnol, and O. Bianchi, "The main blow spun polymer systems: processing conditions and applications," *J. Polym. Res.*, vol. 27, no. 8, pp. 1–23, Aug. 2020.

[8]   G. C. Dadol *et al.*, "Solution blow spinning (SBS) and SBS-spun nanofibers: Materials, methods, and applications," *Mater. Today Commun.*, vol. 25, p. 101656, Dec. 2020.

[9]   D. Gugulothu, A. Barhoum, R. Nerella, R. Ajmer, and M. Bechelany, "Fabrication of Nanofibers: Electrospinning and Non-electrospinning Techniques," *Handb. Nanofibers*, pp. 45–77, 2019.

[10]   J. Song, Z. Li, and H. Wu, "Blowspinning: A New Choice for Nanofibers," *ACS Appl. Mater. Interfaces*, vol. 12, no. 30, pp. 33447–33464, Jul. 2020.

[11]   R. Atif *et al.*, "Study of air pressure and velocity for solution blow spinning of polyvinylidene fluoride nanofibres," *Processes*, vol. 9, no. 6, p. 1014, Jun. 2021.

[12]   A. Kaynak, A. Zolfagharian, and S. Nahavandi, "Finite Element Methods in Smart Materials and Polymers," *Polym. 2020, Vol. 12, Page 1229*, vol. 12, no. 6, p. 1229, May 2020.

[13]   G. Sun, Y. Wang, Y. Zhang, W. Han, and S. Shang, "Formation Mechanism of Fibrous Web in the Solution Blowing Process," *ACS Omega*, vol. 7, no. 24, pp. 20584–20595, Jun. 2022.

[14]   A. Anstey *et al.*, "Nanofibrillated polymer systems: Design, application, and current state of the art," *Prog. Polym. Sci.*, vol. 113, p. 101346, Feb. 2021.

[15]   S. Xie, W. Han, and G. Jiang, "Three dimensional numerical simulation for air flow field in melt blowing," *J. Phys. Conf. Ser.*, vol. 916, no. 1, p. 012044, Oct. 2017.

[16]   M. J. C. de Oliveiraa, R. F. Bonan, S. G. Campos, G. de Araújo Neves, and R. R. Menezes, "Calcium phosphate submicrometric fibers produced by solution blow spinning," *Mater. Res.*, vol. 22, no. 3, p. e20180753, Apr. 2019.

[17]   S. S. Mozafarie and K. Javaherdeh, "Numerical design and heat transfer analysis of a non-Newtonian fluid flow for annulus with helical fins," *Eng. Sci. Technol. an Int. J.*, vol. 22, no. 4, pp. 1107–1115, Aug. 2019.

[18]   W. Han and X. Wang, "Modeling melt blowing fiber with different polymer constitutive equations," *Fibers Polym.*, vol. 17, no. 1, pp. 74–79, Jan. 2016.

[19]   W. Han, S. Xie, X. Sun, X. Wang, and Z. Yan, "Optimization of airflow field via solution blowing for chitosan/PEO nanofiber formation," *Fibers Polym.*, vol. 18, no. 8, pp. 1554–1560, Aug. 2017.

[20]   I. Celik and O. Karatekin, "Numerical Experiments on Application of Richardson Extrapolation With Nonuniform Grids," *J. Fluids Eng. Asme*, vol. 119, no. 3, pp. 584–590, 1997.

[21]   H. Lou, W. Han, and X. Wang, "Numerical Study on the Solution Blowing Annular Jet and Its Correlation with Fiber Morphology," *Ind. Eng. Chem. Res.*, vol. 53, no. 7, pp. 2830–2838, Feb. 2014.

[22]   S. Paudel and N. Saenger, "Grid refinement study for three dimensional CFD model involving incompressible free surface flow and rotating object," *Comput. Fluids*, vol. 143, pp. 134–140, Jan. 2017.

[23]   H. Lou, W. Li, C. Li, and X. Wang, "Systematic investigation on parameters of solution blown micro/nanofibers using response surface methodology based on box-Behnken design," *J. Appl. Polym. Sci.*, vol. 130, no. 2, pp. 1383–1391, Oct. 2013.

[24]   J. L. Daristotle, A. M. Behrens, A. D. Sandler, and P. Kofinas, "A Review of the Fundamental Principles and Applications of Solution Blow Spinning," *ACS Appl. Mater. Interfaces*, vol. 8, no. 51, pp. 34951–34963, Dec. 2016.